PCCP

PAPER

View Article Online
View Journal | View Issue

Cite this: *Phys. Chem. Chem. Phys.*, 2019, **21**, 14033

Direct observation of product-pair correlations in rotationally inelastic collisions of ND_3 with D_2

Zhi Gao,[a] Jérôme Loreau,[b] Ad van der Avoird[a] and Sebastiaan Y. T. van de Meerakker[a]

Received 17th November 2018,
Accepted 8th January 2019

DOI: 10.1039/c8cp07109h

rsc.li/pccp

We present a combined experimental and theoretical study of state-to-state inelastic scattering of $ND_3(j_k^{\pm} = 1_1^-)$ with D_2 (j = 0, 1, 2, 3) molecules at collision energies around 800 cm^{-1}. Using a crossed molecular beam apparatus which employs the combination of Stark deceleration and velocity map imaging, we observe the correlated rotational excitations of both collision partners. For D_2, both elastic ($\Delta j_{D_2} = 0$), inelastic excitation ($j = 0 \rightarrow j = 2$) and inelastic de-excitation ($j = 2 \rightarrow j = 0$) processes are observed. For a number of final ND_3 states, inelastic channels in which D_2 is rotationally excited or de-excited appear surprisingly strong. The experimental results are in excellent agreement with the predictions from quantum scattering calculations which are based on an *ab initio* ND_3–D_2 potential energy surface.

1 Introduction

Obtaining a fundamental understanding of intermolecular interactions is an important objective in physical chemistry. In the past decades, the study of rotational energy transfer in molecular collisional processes has helped us tremendously to probe and understand molecular interactions. These experimental studies have been pivotal to test and develop theory, in order to calculate accurate potential energy surfaces (PESs) and to perform quantum scattering calculations using these PESs.[1–15] Studies of collision energy transfer find applications in various research areas. In astrophysics, for example, the estimation of molecular abundances in the interstellar medium (ISM) from spectral line data requires collisional rate coefficients of various molecules with the most abundant interstellar species such as He, H and H_2.[16]

Compared to atom–molecule systems, the study of molecule–molecule systems is much less mature, and our understanding of bimolecular collisions is rather limited, although significant progress was made recently.[17,18] In bi-molecular collisions, energy transfer between both collision partners can occur, resulting in much more complex collision dynamics compared to atom–molecule collisions. The measurement of rotational energy transfer that occurs in both partners simultaneously, referred to as rotational product-pairs, would yield valuable information on bimolecular scattering processes, and can help us to verify theoretical calculations at an extremely high level.

Experimentally, the velocity map imaging (VMI) technique[19] offers the opportunity to probe product-pairs directly. The idea is that if one can accurately measure the internal state and kinetic energy of one molecular collision partner, one can infer the simultaneous excitation of the unobserved collision partner from a change in kinetic energy of the detected molecule. This method has been pioneered and successfully used in molecular reactive collision experiments,[20–31] in which vibrational product-pairs in the reaction products were probed. For rotationally inelastic scattering, however, the direct observation of rotational product-pairs is challenging, as the typical rotational energy spacing in molecules is rather small, and high image resolutions are required to resolve individual rotational channels in the scattering images.

Recently, using Stark-decelerated molecular beams, Gao *et al.* reported the first direct observation of product-pairs for inelastic collisions between NO radicals and O_2 molecules, at collision energies of 160 cm^{-1} [32] and 480 cm^{-1}.[33] The NO and O_2 molecules have rather similar rotational spacings, and for given final states of NO a series of inelastic transitions in O_2 could be observed. For systems in which the collision partners have very different rotational spacings, such as NO–D_2, the observation of product pairs has to date been elusive, even at collision energies as high as 720 cm^{-1}.[34]

Here, we present the first direct observation of rotational product-pairs for collisions between molecules with very different rotational constants. Using a crossed beam apparatus combining

[a] *Institute for Molecules and Materials, Radboud University, Heyendaalseweg 135, 6525 AJ Nijmegen, The Netherlands. E-mail: basvdm@science.ru.nl*
[b] *Service de Chimie Quantique et Photophysique, Université libre de Bruxelles, CP 160/09, 1050 Brussels, Belgium. E-mail: jloreau@ulb.ac.be*

Stark deceleration and velocity map imaging, we study energy transfer processes in collisions between ND_3 and D_2 molecules at collision energies around 800 cm^{-1}. Compared to NO–O_2, the ND_3–D_2 system is very different, both from a theoretical and experimental perspective. In contrast to NO, the ND_3 molecule has a significant dipole moment, and is a non-linear polyatomic whose rotational levels are characterized by both the rotational quantum number j, and the projection quantum number k. Experimentally, the state-selective ionization detection of ND_3 imparts significant recoil energy to the ions, resulting in a significant blurring of the images that may overshadow product-pair structures. Despite this disadvantage, for selected final states of ND_3, we clearly observe rotational product-pairs, pertaining to both inelastic excitation ($j = 0 \rightarrow 2$) and de-excitation ($j = 2 \rightarrow 0$) processes in D_2. The measured angular and radial distributions of the scattering images are in excellent agreement with the distributions obtained from simulated images which are based on theoretically predicted integral (ICS) and differential cross sections (DCSs).

Rotationally inelastic collisions involving ammonia has attracted considerable interest since the discovery of ammonia in the interstellar medium in 1968 by the observation of emissions from the inversion transitions within the rotational levels $|j_k\rangle = |1_1\rangle$ and $|2_2\rangle$.[35] Observed inversion transitions, in combination with models that take collision-induced population exchange into account, are frequently used to probe the temperature of molecular clouds.[36–38] Rotational energy transfer in collisions of ammonia with various collision partners has been studied by several groups, both with and without selection of the inversion symmetry in the initial state.[39–50]

2 Experimental and theoretical methods

2.1 Experimental set-up

The experiments are performed in a crossed molecular beam apparatus that is schematically shown in Fig. 1, and that has been described in detail before.[32,33] A molecular beam of ND_3 seeded in different carrier gases (Ar, Kr) at a typical pressure of 1 bar is formed using a Nijmegen Pulsed Valve (NPV),[51] and loaded into a 2.6 meter long Stark decelerator. After exiting the decelerator, the packet is scattered with a pulsed beam of neat D_2 at an intersection angle of 90°. The beam of D_2 is produced using a commercially available pulsed valve (Jordan Inc.), and has a mean velocity of 2300 m s^{-1}. In the beam crossing area, the ND_3 molecules are state-selectively ionized by a 2 + 1 Resonance Enhanced Multi Photon Ionization (REMPI) scheme *via* the $\tilde{B} \leftarrow \tilde{X}$ transition using a tunable pulsed dye laser, and subsequently detected by a VMI spectrometer. The VMI detector is calibrated using the method described by Onvlee *et al.*[52] The REMPI process imparts about 20 m s^{-1} recoil velocity to the ions, resulting in a reduction of image resolution.

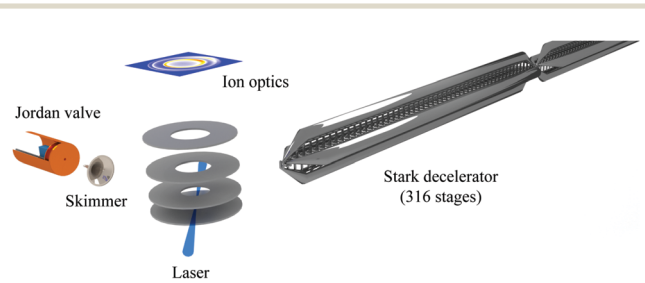

Fig. 1 Schematic representation of the experimental set-up. A packet of ND_3 is quantum state selected and velocity controlled by a 2.6 m long Stark decelerator, and scattered with a pulsed beam of neat D_2 at 90° angle of incidence. The inelastically scattered ND_3 molecules are state-selectively ionized using a pulsed laser, and recorded using a standard velocity map imaging detector. Only the last section of the Stark decelerator is shown.

In the experiments, we use the Stark decelerator in two different modes of operation. In the first, we use Ar as a carrier gas and operate the decelerator to guide the ND_3 through the decelerator at a constant speed of 610 m s^{-1}. This mode of operation yields the highest particle density for the ND_3 packet, but also the largest velocity spread and corresponding lowest image resolutions. In the second, we use Kr as a carrier gas and operate the Stark decelerator to slow a packet of ND_3 to a final velocity of 306 m s^{-1}.[53] The deceleration process reduces the particle density, but improves the velocity spread of the packet and the resolution in the scattering images. We therefore refer to these modes below as high density mode and high resolution mode, respectively. The collision energy is very similar in both modes and amounts to 800 cm^{-1} and 750 cm^{-1} for the high density and high resolution modes, respectively.

The ground state of ND_3 has a pyramidal (C_{3v}) equilibrium geometry. Due to the "umbrella" vibrational mode and the double-minimum potential along the inversion coordinate, all the rotational levels of ND_3 split into doublets where the upper and lower components have negative and positive parity, respectively. The rotational levels of ND_3 are denoted by j_k where j represents the angular momentum and k is the projection of j on the C_3 axis. The rotational energy level diagrams of ND_3 and D_2 are shown in Fig. 2. Only the rotational levels involved in this experiment are shown. The D_2 molecule has a symmetric wave function under permutations of the two identical nuclei, deuterons, having a nuclear spin $I = 1$.[54] As a result, D_2 molecules exist in two different nuclear spin configurations, namely *ortho* ($I_{total} = 0$ or 2) and *para* ($I_{total} = 1$) where I_{total} denotes the total nuclear spin which can take the values 0, 1 or 2. *ortho* and *para*-D_2 correspond to rotational states for which the rotational wave function is symmetric (j_{D_2} = even) and anti-symmetric (j_{D_2} = odd) under permutation of the nuclei, respectively.

Before the collision, more than 99.5% of ND_3 resides in the upper inversion level of the 1_1 state (1_1^-). As discussed by Tkáč *et al.*,[42] the ND_3 molecule exists in three nuclear spin modifications. Since the selected 1_1^- level has E symmetry, only final states which also have E symmetry can be observed in our experiments. Since we used normal D_2 in this experiment, various initial states of D_2 are populated in the molecular beam. The populations in these states were probed using REMPI at room temperature (see Fig. 3), from which we can

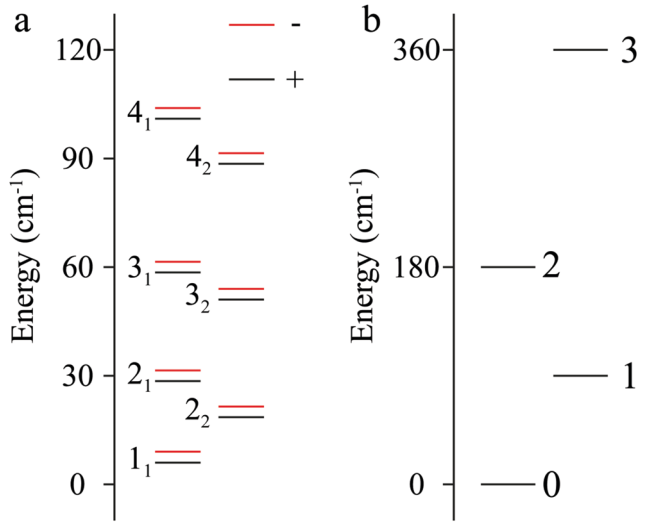

Fig. 2 (a) The energy level diagram of *para*-ND_3. The inversion splitting of each rotational level is exaggerated for clarity. The upper and lower inversion component of each rotational level has negative and positive parity, respectively. (b) The energy level diagram of D_2. Levels with j = even and j = odd belong to *ortho*-D_2 and *para*-D_2, respectively.

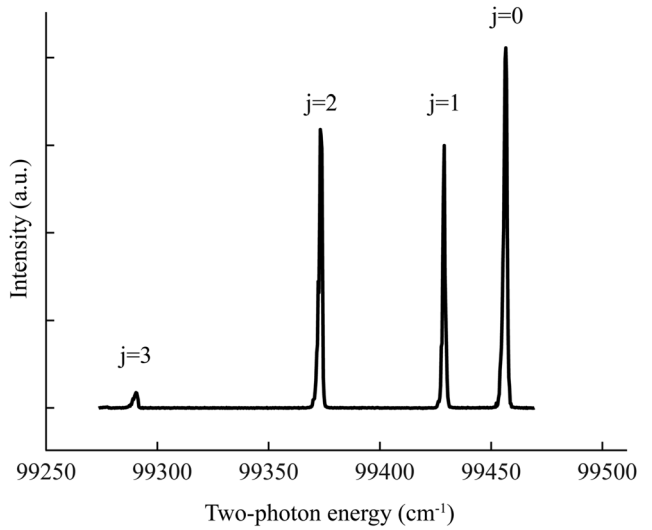

Fig. 3 Assigned REMPI spectrum of a neat beam of D_2 to probe the initial populations in the D_2 beam.

estimate that before the collision about 37%, 28%, 30%, and 5% of the D_2 molecules reside in the j = 0, 1, 2, and 3 levels, respectively. The minor initial population in j = 3 is not relevant for the experiments reported here, and will be further neglected. In collisions, population transfer between *o*-D_2 and *p*-D_2 is forbidden, such that only j_{D_2} = even → j_{D_2} = even and j_{D_2} = odd → j_{D_2} = odd transitions are allowed.

The experimental results are compared with cross sections predicted by theory. For this, we simulate scattering images based on the cross sections from the quantum scattering calculations and the accurately known experimental conditions. The blurring due to ion recoil imparted by the ND_3 detection is taken into account in these simulations. We then directly compare the radial and angular distributions of the scattering intensity in both the experimental and simulated images. The details about the simulation and analysis methods are described elsewhere,[32,33] and will not be discussed here. The advantage of this procedure is that we do not have to rely on extensive fitting procedures to extract cross sections from our images, which can be prone to error and misinterpretation of the results. The disadvantage of the method is that we do not directly compare measured cross sections with the calculated ones.

2.2 Quantum scattering calculations for ND_3–D_2

Quantum scattering calculations were performed on the five-dimensional NH_3–H_2 potential energy surface (PES) of Maret *et al.*[55] The PES depends on the coordinates R (the length of the vector **R** connecting the NH_3 and H_2 centers of mass), θ_1 (the angle between R and the C_3 axis of NH_3), ϕ_1 (the angle of rotation of this vector around the C_3 axis), and (θ_2, ϕ_2), which are the polar and azimuthal angles used to describe the orientation of H_2 relative to NH_3. Both molecules are thus assumed to be rigid rotors.

The PES was constructed[55] by computing the energy for 89 000 nuclear geometries with the coupled-cluster method with single, double, and perturbative triple excitations [CCSD(T)] and the aug-cc-pVDZ basis set. These energies were calibrated using a complete basis set extrapolation procedure based on a set of 29 000 points calculated with the larger aug-cc-pVTZ basis set. The resulting PES has an estimated accuracy of about 1 cm^{-1}. The accuracy of the PES was previously assessed in molecular beam[50] and spectroscopic[56] experiments. At each distance R, the energy was expanded in terms of a set of angular functions as

$$V(R,\theta_1,\phi_1,\theta_2,\phi_2) = \sum_{l_1\mu_1 l_2 l} v_{l_1\mu_1 l_2 l}(R)\, t_{l_1\mu_1 l_2 l}(\theta_1,\phi_1,\theta_2,\phi_2), \quad (1)$$

where the angular functions $t_{l_1\mu_1 l_2 l}$ are given in ref. 57. The radial functions were fitted using cubic splines and extrapolated to large R with the appropriate R^{-n} behaviour.

We assume here that the ND_3–D_2 system can be described with the same PES as NH_3–H_2. This PES was expressed in different coordinates, however, to take into account the shift in the position of the center of mass of ND_3 with respect to NH_3, as discussed in ref. 58. This transformation affects the coordinates R and θ_1, and the PES was re-expanded according to eqn (1) in terms of the new coordinates (R',θ_1',ϕ_1,θ_2,ϕ_2). The expansion coefficients $v_{l_1\mu_1 l_2 l}(R')$ were computed up to l_1 = 11 and l_2 = 4.

Quantum scattering calculations of integral and differential cross sections for ND_3–D_2 collisions were carried out with an in-house scattering code[59] that implements the close-coupling method for symmetric top – linear molecule collisions.[60] State-to-state cross sections were computed at two collision energies (750 cm^{-1} and 800 cm^{-1}) for the initial states $ND_3(1_1^-)$ + $D_2(j)$, where j = 0, 1, 2, 3. The rotational basis for the close-coupling calculations consisted of all *para* rotational states of ND_3 with $j \leq 10$, all *ortho* states with $j \leq 4$ of D_2 for collisions of ND_3 with $D_2(0)$ or $D_2(2)$, all *para* states with $j \leq 3$ of D_2 for collisions

with $D_2(1)$, and all *para* states with $j \leq 5$ of D_2 for collisions with $D_2(3)$. The rotational constant of D_2 was taken as B = 30.443 cm^{-1}, while the rotational constants of ND_3 were taken as A = 5.1432 cm^{-1} and C = 3.1015 cm^{-1}. The inversion splitting between in the ground umbrella vibrational state was 0.0530 cm^{-1}. Since the PES does not describe the inversion of ND_3, the umbrella motion was treated with a two-state model in which the ground inversion-tunnelling states are taken as linear combinations of the two rigid equilibrium states. This model was shown to be in excellent agreement with results obtained by treating the umbrella motion of ammonia explicitly for the scattering of NH_3 with rare gas atoms.[61]

The calculations were performed on a grid of 115 values of R' in the range 3.5–25 a_0. Partial waves with total angular momenta up to J = 70 were considered, and the convergence of the cross sections was checked with respect to all the parameters discussed above.

3 Results and discussion

3.1 High density mode

A broad range of final states can experimentally be probed when the Stark decelerator is operated in the high density mode. Fig. 4 shows a collection of experimental scattering images for inelastic collisions in which ND_3 molecules are excited into both inversion components of the final states 2_1, 2_2, 3_1, 3_2, 4_1 and 4_2. In most of the images, up to three concentric rings can be seen which correspond to different rotational transitions of D_2 during the collision. The most intense ring, which coincides with the masked beam spot,[32] corresponds to the elastic D_2 channels, *i.e.*, in these collisions the D_2 molecules remain in their initial quantum state. The three elastic $j = 0 \rightarrow 0$, $j = 1 \rightarrow 1$ and $j = 2 \rightarrow 2$ channels all have the same ring radius and are superimposed in the image. At slightly smaller radii, a clear inelastic channel is visible that is peaked in a narrow window of scattering angles around forward scattering. This channel corresponds to inelastic $j = 0 \rightarrow 2$ rotational excitation transitions in D_2. At slightly larger radii, a third inelastic channel is visible, pertaining to rotational $j = 2 \rightarrow 0$ de-excitation collisions. Both assignments are confirmed from the radial scattering distributions *vide infra* in combination with the rotational energy level structure of D_2. Note that no indications are found for inelastic $j = 1 \rightarrow 3$ rotational excitation transitions, although a significant initial population in $j = 1$ is present and the transition energy is well within the collision energy of the experiment.

3.2 High resolution mode

In order to take a closer look at the three individual scattering channels, selected images were measured again using the Stark decelerator in high resolution mode. The upper and lower inversion component of the final state 3_1 were selected for this, as this scattering channel has a relatively high integral cross section. The experimental scattering images are shown on the left side of Fig. 6. Indeed, the three scattering channels are observed with a slightly better resolution compared to the images shown in Fig. 4, although the improvement in resolution is only marginal. This is the consequence of the image blurring due to the ion recoil velocity imparted by the REMPI detection process, which dominates the image resolution in the present experiments irrespective of the velocity spreads of the incoming beams.

3.3 Comparison with theory

To compare the experimental results with theory, scattering images are simulated based on the kinematics of the experiment and the cross sections derived from the scattering calculations. The resulting simulated scattering images are shown in Fig. 5, and for the two high-resolution images in Fig. 6. To facilitate a more quantitative comparison, the radial and angular distributions are extracted from both the experimental and simulated images, and shown in Fig. 7 and 8, respectively. The distributions of the high-resolution images from Fig. 6 are shown in Fig. 9 and 10.

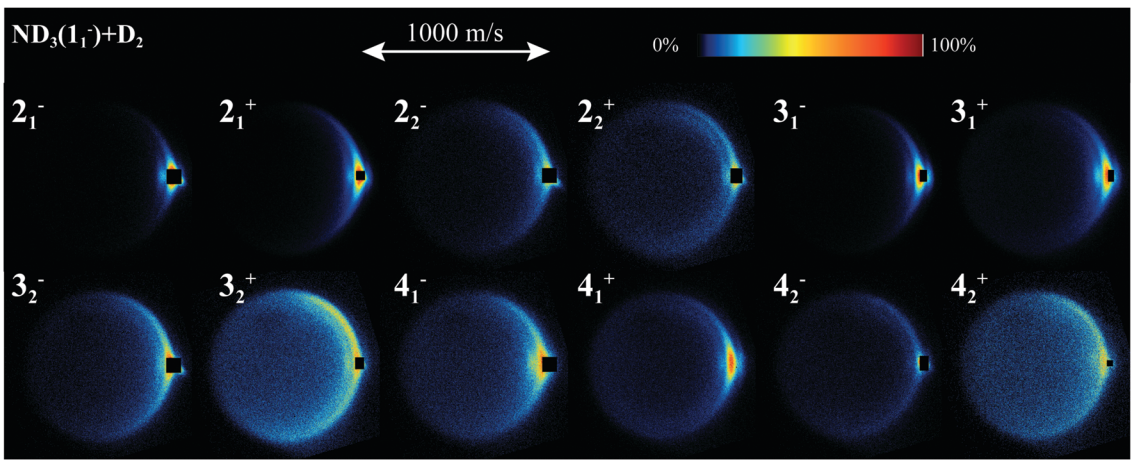

Fig. 4 Experimental scattering images for ND_3–D_2 collisions at a collision energy of 800 cm^{-1}. The final states of ND_3 are probed and labelled in each image. All images are presented such that the relative velocity vector is oriented horizontally and forward scattering appears on the righthand side of each image. A small section of the images near forward scattering is masked due to imperfect state selection of the initial ND_3 packet.

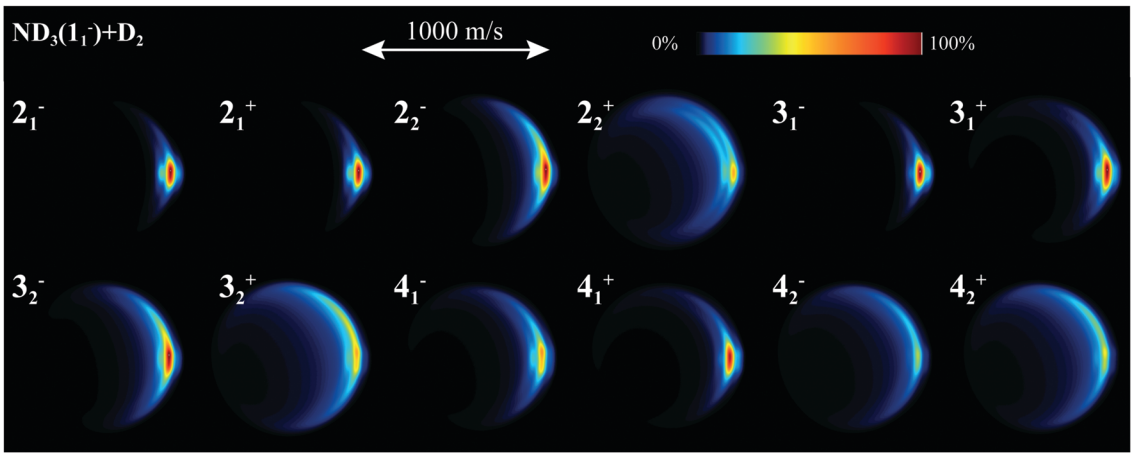

Fig. 5 Simulates scattering images for ND_3–D_2 collisions at a collision energy of 800 cm^{-1}, corresponding to the experimental images of Fig. 4.

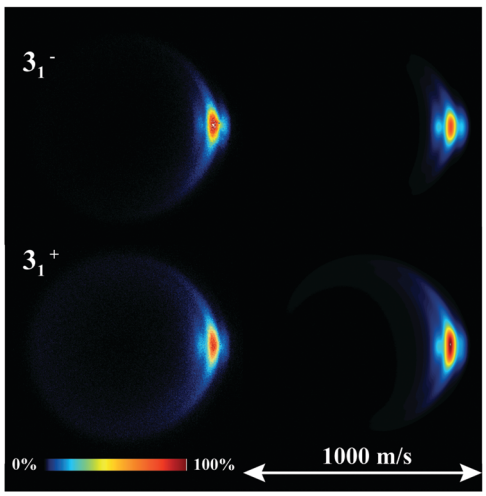

Fig. 6 Experimental (left) and simulated (right) scattering images for $ND_3(1_1^-)$ + D_2 → $ND_3(3_1^-, 3_1^+)$ + D_2 inelastic collisions at a collision energy of 750 cm^{-1}. The Stark decelerator is operated in high resolution mode to obtain the experimental images.

In the radial distributions, the positions at which the elastic, inelastic $j = 0 \rightarrow 2$ excitation as well as the inelastic $j = 2 \rightarrow 0$ de-excitation transitions are expected based on the kinematics of the experiment are indicated by vertical dashed lines. For those states where a clear inelastic excitation or de-excitation channel for D_2 was not observed, the corresponding vertical traces were omitted.

It is seen that near-perfect agreement between experiment and simulations is obtained for almost all images, both regarding the radial and the angular distributions. The angular distributions, as well as the intensity ratios between elastic and inelastic D_2 channels for given final states of ND_3 are well reproduced by the simulations. This indicates that the scattering calculations capture the scattering dynamics well.

Some interesting trends can be observed in the images. First, most scattering channels display a predominantly forward scattered behaviour, with the exception of 2_2^+, 3_2^+ and 4_2^+ final states that have a significant component toward side-scattered angles. Secondly, the inelastic D_2 channels have surprisingly large intensities compared to the corresponding elastic channels, considering the relatively large amount of rotational energy that is transferred in an inelastic event. It should be noted here that, since we always cut out the beamspots at the forward direction in our analysis, the scattering signals (mostly the $j = 2 \rightarrow 0$ de-excitation channel of D_2) which overlap with the beamspots are also cut out. That is the reason why

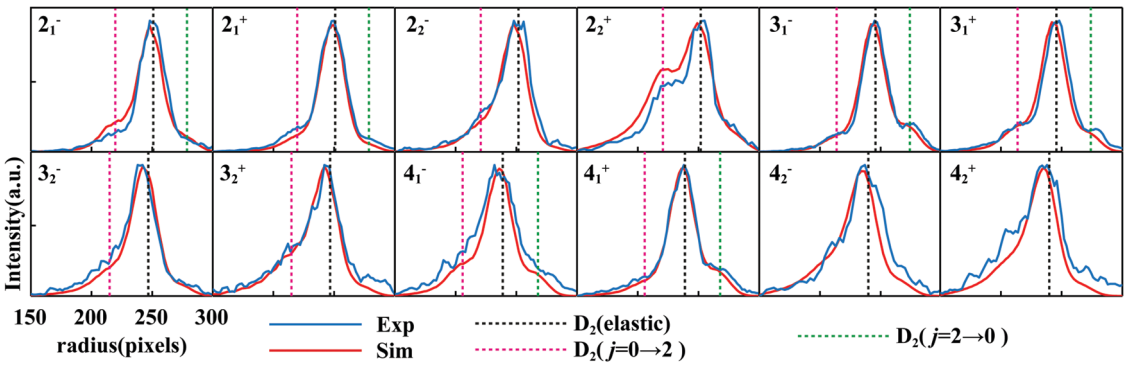

Fig. 7 Radial distributions for the experimental scattering images in Fig. 4 (exp), and the corresponding simulated images from Fig. 5 (sim). The different rotational transitions of D_2 are labelled by the dashed lines.

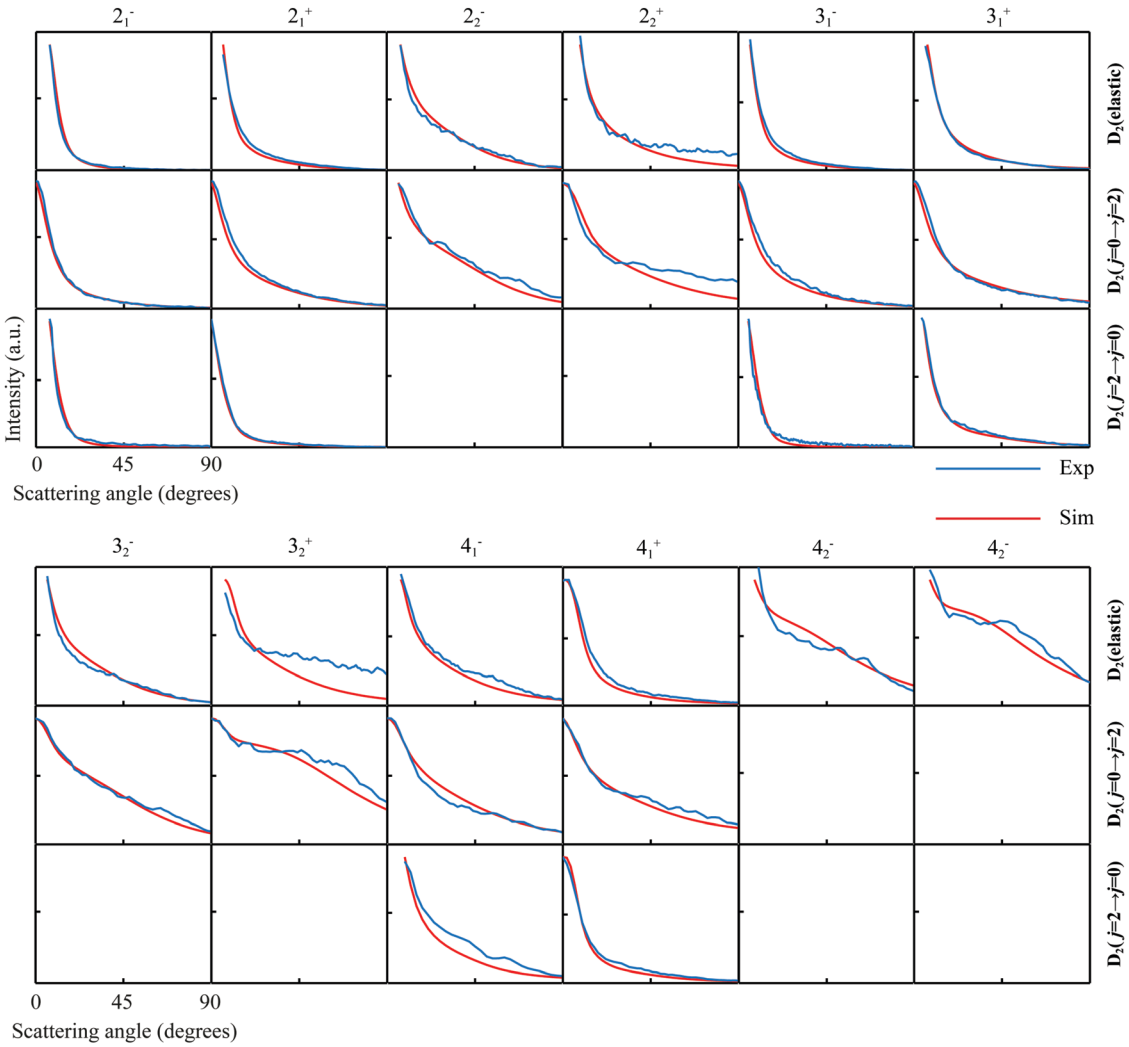

Fig. 8 Angular distributions for the experimental scattering images in Fig. 4 (exp), and the corresponding simulated images from Fig. 5 (sim). The final states of ND_3 and rotational transitions of D_2 are labelled. For those final ND_3 states where a clear inelastic excitation or de-excitation channel for D_2 was not observed, the corresponding panels were left empty.

in some scattering channels of ND_3, we could not observe the accompanying de-excitation channel of D_2.

In comparison with our previous NO–D_2 inelastic scattering results,[34] D_2 shows much stronger rotational (de-)excitation when it collides with ND_3. This can be explained by the role of the dipole and quadrupole moments of ND_3, which are larger than those of NO by about an order of magnitude. Fig. 11 shows the radial expansion coefficients $v_{l_1\mu_1 l_2 l}(R)$ of the ND_3–D_2 interaction potential. The dominant anisotropic terms over a large range of R-values are the 1023 and 2024 terms that correspond to the electrostatic interactions between the dipole and quadrupole of ND_3 and the quadrupole of D_2. These interactions, which decay as R^{-4} and R^{-5}, are also dominant in the long range, because all other terms decay as R^{-n} with $n \geq 6$. Fig. 12 and 13 show integral cross sections (ICSs) calculated with different terms included in the potential. They illustrate that these electrostatic interaction terms largely determine the cross sections of the $j = 0 \rightarrow 2$ excitation and $j = 2 \rightarrow 0$ de-excitation transitions in D_2. In other words, the dipole–quadrupole and quadrupole–quadrupole interactions play a dominant role in the rotational (de-)excitation of D_2 when it collides with ND_3.

Another striking observation, illustrated in Fig. 8, is that the $j = 0 \rightarrow 2$ and $j = 2 \rightarrow 0$ (de-)excitation transitions of D_2 occur prominently for final j_k states of ND_3 with $k = 1$, while they are much weaker for final states with $k = 2$. Also this can be explained by considering the anisotropic expansion of the potential shown in Fig. 11. The initial $j_k = 1_1^-$ state of ND_3 is coupled to final states with $k = 1$ by all terms in the potential with $\mu_1 = 0$, which include the dominant 1023 and 2024 electrostatic terms mentioned in the preceding paragraph. Final states with $k = 2$ are coupled to the initial $k = 1$ state by the terms with $\mu_1 = 3$. This can be understood by realizing that k and μ_1 represent the absolute values of the actual k and μ_1 quantum numbers. Terms with $\mu_1 = \pm 3$ couple states with $k = 1$ to states with $k = \pm 2$. Since the anisotropic interaction terms

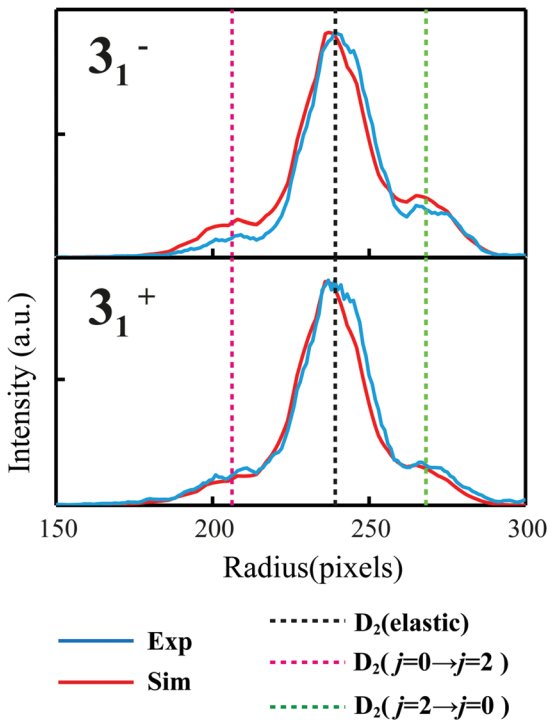

Fig. 9 Radial distributions for the experimental and simulated scattering images in Fig. 6. The different rotational transitions of D_2 are indicated by the dashed lines.

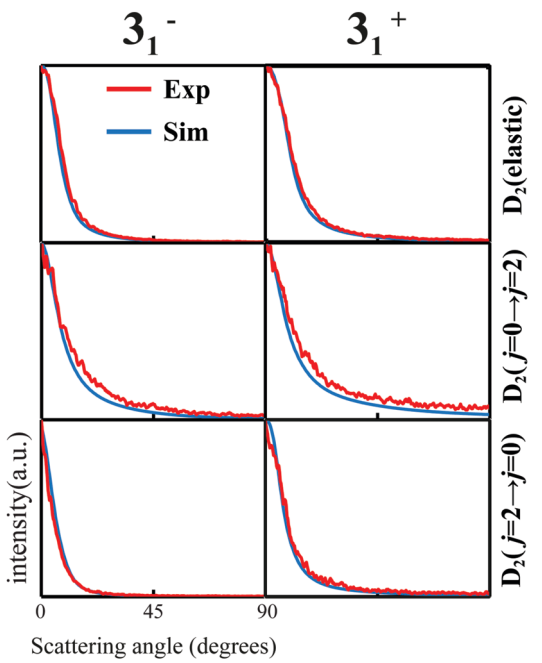

Fig. 10 Angular distributions for the experimental and simulated scattering images in Fig. 6. The different rotational transitions of D_2 are labelled on the vertical axis on the right.

with $\mu_1 = 3$ are much smaller than the terms with $\mu_1 = 0$, see Fig. 11, this explains the more prominent (de-)excitation of D_2 accompanying transitions to the ND_3 final states with $k = 1$.

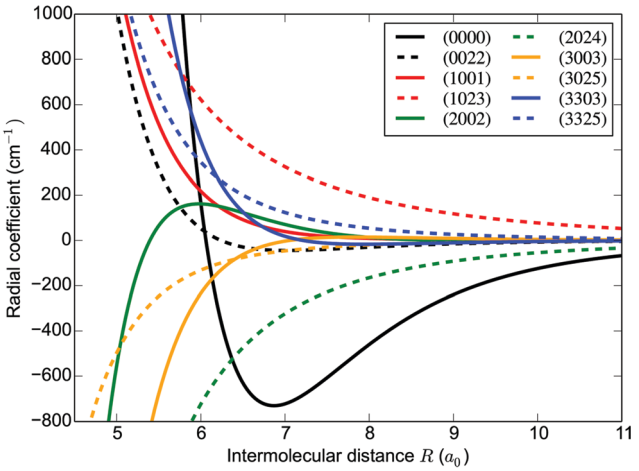

Fig. 11 Radial expansion coefficients $v_{l_1\mu_1 l_2 l}(R)$ of the ND_3–D_2 interaction potential. The curve labelled 0000 is the isotropic interaction potential, the other curves are the different anisotropic contributions.

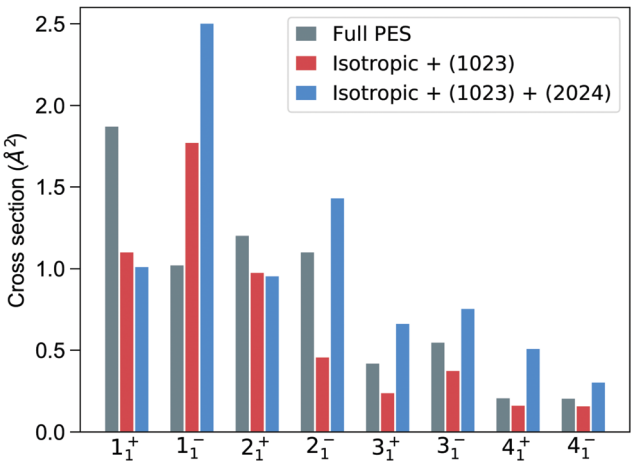

Fig. 12 Comparison of calculated ICSs for D_2 ($j = 0$) → D_2 ($j = 2$). Three different potentials were used in the calculations [gray: full PES, red: isotropic + dipole–quadrupole (1 0 2 3) terms, blue: isotropic + dipole–quadrupole + quadrupole–quadrupole (2 0 2 4) terms]. The final states of ND_3 are labelled below the bars.

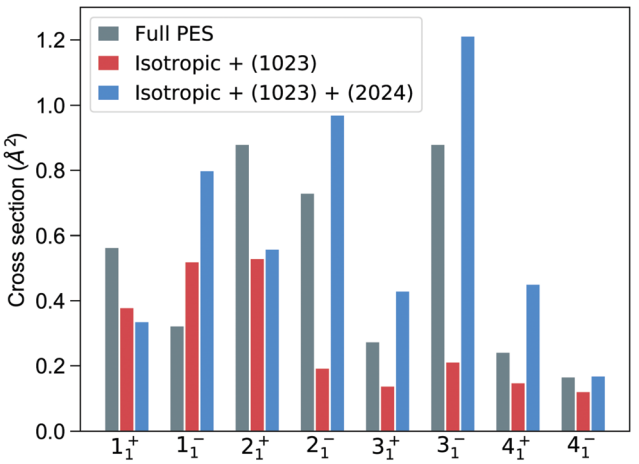

Fig. 13 Comparison of calculated ICSs for D_2 ($j = 2$) → D_2 ($j = 0$). For the labelling, see Fig. 12.

4 Conclusion

We presented high-resolution measurements of rotational product-pairs for inelastic collisions between state-selected and velocity controlled ND_3 molecules and D_2 molecules at collision energies around 800 cm^{-1}. Many final rotational states of ND_3 were studied. For a number of ND_3 final states we found interesting trends in the pair-correlated state-to-state cross sections: not only collisions elastic in D_2 were observed, but also collisions in which D_2 is excited or de-excited with $\Delta j = \pm 2$. The experimental results are compared to quantum scattering calculations using an *ab initio* ND_3–D_2 potential energy surface. Excellent agreement between experiment and theory is found throughout, indicating that the potential energy surface is accurate and the scattering calculations capture pair-correlated processes in bimolecular collisions well.

The resolution in the current experiments is limited by the REMPI detection scheme for ND_3, which imparts a relatively large recoil energy to the ions, thereby significantly blurring the scattering images. This prohibits the observation of diffraction oscillations in the angular scattering distributions, for instance, which would constitute a further stringent test for theory. This inherent limitation can be overcome if a sensitive, state-selective recoil-free REMPI scheme becomes available.

Conflicts of interest

The authors declare no competing financial interest.

Acknowledgements

The research leading to these results has received funding from the European Research Council under the European Union's Seventh Framework Programme (FP7/2007-2013)/ERC grant agreement 335646 MOLBIL. This work is part of the research program of the Netherlands Organization for Scientific Research (NWO). The expert technical support by Niek Janssen, André van Roij, and Edwin Sweers is gratefully acknowledged.

References

1 A. von Zastrow, J. Onvlee, S. N. Vogels, G. C. Groenenboom, A. van der Avoird and S. Y. T. van de Meerakker, *Nat. Chem.*, 2014, **6**, 216–221.
2 M. Brouard, H. Chadwick, S. D. S. Gordon, B. Hornung, B. Nichols, F. J. Aoiz and S. Stolte, *J. Chem. Phys.*, 2016, **144**, 224301.
3 J. Onvlee, S. N. Vogels, A. van der Avoird, G. C. Groenenboom and S. Y. T. van de Meerakker, *New J. Phys.*, 2015, **17**, 055019.
4 J. J. Kay, J. D. Steill, J. Kłos, G. Paterson, M. L. Costen, K. E. Strecker, K. G. McKendrick, M. H. Alexander and D. W. Chandler, *Mol. Phys.*, 2012, **110**, 1693–1703.
5 S. N. Vogels, J. Onvlee, S. Chefdeville, A. van der Avoird, G. C. Groenenboom and S. Y. T. van de Meerakker, *Science*, 2015, **350**, 787–790.
6 M. Brouard, H. Chadwick, S. D. S. Gordon, B. Hornung, B. Nichols, F. J. Aoiz and S. Stolte, *J. Phys. Chem. A*, 2015, **119**, 12404–12416.
7 M. Brouard, H. Chadwick, C. J. Eyles, B. Hornung, B. Nichols, J. M. Scott, F. J. Aoiz, J. Kłos, S. Stolte and X. Zhang, *Mol. Phys.*, 2013, **111**, 1759–1771.
8 M. Brouard, H. Chadwick, C. J. Eyles, B. Hornung, B. Nichols, F. J. Aoiz, P. G. Jambrina and S. Stolte, *J. Chem. Phys.*, 2013, **138**, 104310.
9 A. Gijsbertsen, H. Linnartz, G. Rus, A. E. Wiskerke, S. Stolte, D. W. Chandler and J. Kłos, *J. Chem. Phys.*, 2005, **123**, 224305.
10 J. J. van Leuken, F. H. W. V. Amerom, J. Bulthuis, J. G. Snijders and S. Stolte, *J. Phys. Chem.*, 1995, **99**, 15573–15579.
11 B. Nichols, H. Chadwick, S. D. S. Gordon, C. J. Eyles, B. Hornung, M. Brouard, M. H. Alexander, F. J. Aoiz, A. Gijsbertsen and S. Stolte, *Chem. Sci.*, 2015, **6**, 2202–2210.
12 A. Bergeat, S. Chefdeville, M. Costes, S. B. Morales, C. Naulin, U. Even, J. Kłos and F. Lique, *Nat. Chem.*, 2018, **10**, 519–522.
13 A. Bergeat, J. Onvlee, C. Naulin, A. van der Avoird and M. Costes, *Nat. Chem.*, 2015, **7**, 349–353.
14 S. Chefdeville, Y. Kalugina, S. Y. T. van de Meerakker, C. Naulin, F. Lique and M. Costes, *Science*, 2013, **341**, 1094–1096.
15 S. Chefdeville, T. Stoecklin, A. Bergeat, K. M. Hickson, C. Naulin and M. Costes, *Phys. Rev. Lett.*, 2012, **109**, 023201.
16 J. Kłos and F. Lique, *Theoretical and Computational Chemistry Series*, Royal Society of Chemistry, 2017, pp. 46–91.
17 C.-H. Yang, G. Sarma, D. H. Parker, J. J. ter Meulen and L. Wiesenfeld, *J. Chem. Phys.*, 2011, **134**, 204308.
18 G. Sarma, C.-H. Yang, A. K. Saha, D. H. Parker and L. Wiesenfeld, *J. Chem. Phys.*, 2013, **138**, 024314.
19 A. T. J. B. Eppink and D. H. Parker, *Rev. Sci. Instrum.*, 1997, **68**, 3477–3484.
20 H. Pan, K. Liu, A. Caracciolo and P. Casavecchia, *Chem. Soc. Rev.*, 2017, **46**, 7517–7547.
21 H. Pan, F. Wang, G. Czakó and K. Liu, *Nat. Chem.*, 2017, **9**, 1175–1180.
22 W. Dong, C. Xiao, T. Wang, D. Dai, X. Yang and D. H. Zhang, *Science*, 2010, **327**, 1501–1502.
23 T. Wang, J. Chen, T. Yang, C. Xiao, Z. Sun, L. Huang, D. Dai, X. Yang and D. H. Zhang, *Science*, 2013, **342**, 1499–1502.
24 T. Yang, J. Chen, L. Huang, T. Wang, C. Xiao, Z. Sun, D. Dai, X. Yang and D. H. Zhang, *Science*, 2015, **347**, 60–63.
25 J. Zhou, J. J. Lin and K. Liu, *J. Chem. Phys.*, 2003, **119**, 8289–8296.
26 J. J. Lin, J. Zhou, W. Shiu and K. Liu, *Science*, 2003, **300**, 966–969.
27 J. Zhou, W. Shiu, J. J. Lin and K. Liu, *J. Chem. Phys.*, 2004, **120**, 5863–5866.
28 W. Shiu, J. J. Lin, K. Liu, M. Wu and D. H. Parker, *J. Chem. Phys.*, 2004, **120**, 117–122.
29 J. Zhou, W. Shiu, J. J. Lin and K. Liu, *J. Chem. Phys.*, 2006, **124**, 104309.
30 K. Liu, *Phys. Chem. Chem. Phys.*, 2007, **9**, 17–30.

31 Y.-T. Wu and K. Liu, *J. Chem. Phys.*, 2008, **129**, 154302.
32 Z. Gao, T. Karman, S. N. Vogels, M. Besemer, A. van der Avoird, G. C. Groenenboom and S. Y. T. van de Meerakker, *Nat. Chem.*, 2018, **10**, 469–473.
33 Z. Gao, T. Karman, G. Tang, A. van der Avoird, G. C. Groenenboom and S. Y. T. van de Meerakker, *Phys. Chem. Chem. Phys.*, 2018, **20**, 12444–12453.
34 Z. Gao, S. N. Vogels, M. Besemer, T. Karman, G. C. Groenenboom, A. van der Avoird and S. Y. T. van de Meerakker, *J. Phys. Chem. A*, 2017, **121**, 7446–7454.
35 A. C. Cheung, D. M. Rank, C. H. Townes, D. D. Thornton and W. J. Welch, *Phys. Rev. Lett.*, 1968, **21**, 1701–1705.
36 C. M. Walmsley and H. Ungerechts, *Astron. Astrophys.*, 1983, **122**, 164–170.
37 F. Daniel, C. Rist, A. Faure, E. Roueff, M. Gérin, D. C. Lis, P. Hily-Blant, A. Bacmann and L. Wiesenfeld, *Mon. Not. R. Astron. Soc.*, 2016, **457**, 1535–1549.
38 N. Bouhafs, C. Rist, F. Daniel, F. Dumouchel, F. Lique, L. Wiesenfeld and A. Faure, *Mon. Not. R. Astron. Soc.*, 2017, **470**, 2204–2211.
39 H. Meyer, *J. Phys. Chem.*, 1995, **99**, 1101–1114.
40 J. Schleipen and J. ter Meulen, *Chem. Phys.*, 1991, **156**, 479–496.
41 G. C. M. van der Sanden, P. E. S. Wormer and A. van der Avoird, *J. Chem. Phys.*, 1996, **105**, 3079–3088.
42 O. Tkáč, A. K. Saha, J. Onvlee, C.-H. Yang, G. Sarma, C. K. Bishwakarma, S. Y. T. van de Meerakker, A. van der Avoird, D. H. Parker and A. J. Orr-Ewing, *Phys. Chem. Chem. Phys.*, 2014, **16**, 477–488.
43 H. Meyer, U. Buck, R. Schinke and G. H. F. Diercksen, *J. Chem. Phys.*, 1986, **84**, 4976–4987.
44 A. Das and C. H. Townes, *J. Chem. Phys.*, 1986, **85**, 179–189.
45 P. W. Daly and T. Oka, *J. Chem. Phys.*, 1970, **53**, 3272–3278.
46 T. Oka, *J. Chem. Phys.*, 1968, **48**, 4919–4928.
47 T. Oka, *J. Chem. Phys.*, 1968, **49**, 3135–3145.
48 M. Broquier, A. Picard-Bersellini and J. Hall, *Chem. Phys. Lett.*, 1987, **136**, 531–534.
49 O. Tkáč, A. K. Saha, J. Loreau, D. H. Parker, A. van der Avoird and A. J. Orr-Ewing, *J. Phys. Chem. A*, 2015, **119**, 5979–5987.
50 O. Tkáč, A. K. Saha, J. Loreau, Q. Ma, P. J. Dagdigian, D. H. Parker, A. van der Avoird and A. J. Orr-Ewing, *Mol. Phys.*, 2015, **113**, 3925–3933.
51 B. Yan, P. F. H. Claus, B. G. M. van Oorschot, L. Gerritsen, A. T. J. B. Eppink, S. Y. T. van de Meerakker and D. H. Parker, *Rev. Sci. Instrum.*, 2013, **84**, 023102.
52 J. Onvlee, S. N. Vogels, A. von Zastrow, D. H. Parker and S. Y. T. van de Meerakker, *Phys. Chem. Chem. Phys.*, 2014, **16**, 15768–15779.
53 S. N. Vogels, Z. Gao and S. Y. T. van de Meerakker, *EPJ Tech. Instrum.*, 2015, **2**, 1.
54 C.-Y. Liu, S. Lamoreaux, A. Saunders, D. Smith and A. Young, *Nucl. Instrum. Methods Phys. Res., Sect. A*, 2003, **508**, 257–267.
55 S. Maret, A. Faure, E. Scifoni and L. Wiesenfeld, *Mon. Not. R. Astron. Soc.*, 2009, **399**, 425.
56 L. A. Surin, I. V. Tarabukin, S. Schlemmer, A. A. Breier, T. F. Giesen, M. C. McCarthy and A. van der Avoird, *Astrophys. J.*, 2017, **838**, 27.
57 T. Phillips, S. Maluendes, A. McLean and S. Green, *J. Chem. Phys.*, 1994, **101**, 5824.
58 Q. Ma, A. van der Avoird, J. Loreau, M. Alexander, S. Y. T. van de Meerakker and P. J. Dagdigian, *J. Chem. Phys.*, 2015, **143**, 044312.
59 K. B. Gubbels, S. Y. T. van de Meerakker, G. C. Groenenboom, G. Meijer and A. van der Avoird, *J. Chem. Phys.*, 2012, **136**, 074301.
60 A. Offer and D. R. Flower, *J. Phys. B: At., Mol. Opt. Phys.*, 1989, **22**, L439.
61 J. Loreau and A. van der Avoird, *J. Chem. Phys.*, 2015, **143**, 184303.